Atomistic Simulations of Laser-controlled Exciton Transfer and Stabilization in Symmetric Double Quantum Dots

Pascal Krause[1,2], Jean Christophe Tremblay[3], Annika Bande[1*,†]

†[1] *Theory of Electron Dynamics and Spectroscopy, Helmholtz-Zentrum Berlin für Materialien und Energie GmbH, Hahn-Meitner Platz 1, 14109 Berlin, Germany*

‡[2] *Physical and Theoretical Chemistry, Institute of Chemistry and Biochemistry Freie Universität Berlin, Arnimallee 22, 14195 Berlin*

¶[3] *Laboratoire de Physique et Chimie Théoriques, UMR7019, CNRS-Université de Lorraine, 1 Bd Arago, 57070 Metz, France*

E-mail: pascal.krause@helmholtz-berlin.de

Abstract

The creation, transfer, and stabilization of localized excitations is studied in a donor-acceptor Frenkel exciton model in an atomistic treatment of reduced-size double quantum dots of various sizes. The explicitly time-dependent dynamics simulations carried out by hybrid time-dependent density functional theory/configuration interaction show that laser-controlled hole trapping in stacked, coupled germanium/silicon quantum dots can be achieved by an UV/IR pump-dump pulse sequence. The first UV excitation creates an exciton localized on the topmost QD and after some coherent transfer time an IR pulse dumps and localize an exciton in the bottom QD. While hole trapping is observed in each excitation step, we show that the stability of the localized electron depends on its multi-excitonic character. We present how size and geometry variations of three Ge/Si nanocrystals influences transfer times and thus the efficiency of laser-driven populations of the electron-hole pair states.

Graphical TOC Entry

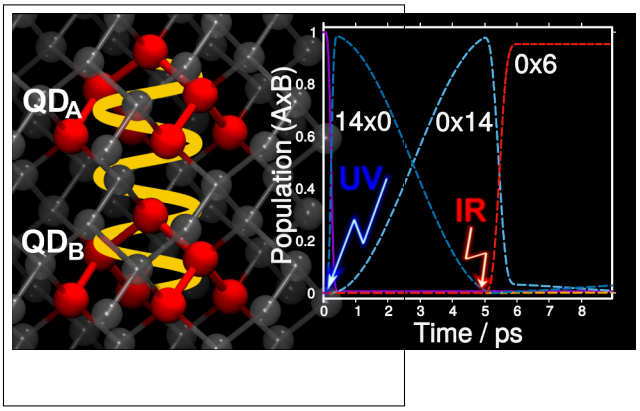

Introduction

With miniaturization becoming ever more important in technology, nanotechnology became an emergent field in the recent years, in which nanometer-sized components are designed with respect to their size, morphology, and chemical composition to have desired properties. One class of nanoparticles made from a few hundreds of atoms of semiconducting materials like silicon, gallium or arsenic, is quantum dots (QDs).[1,2] They are attractive for their size-tunable band gap[3,4] and the discrete states for their charge carriers, which are significantly different from that of the respective bulk materials.[4]

QDs exist in a vast range of structural realizations arising from different fabrication routes.[5] Some methods obtain QDs from thin films[6] or nanowires[7] with subsequent electrostatic confinement of the charge carriers. Others use detonation to decompose larger particles into nanoparticles.[8] A large domain, however, is the growth of structures under different conditions: in colloidal solution,[9] in wires with alternating materials,[10] on etched surfaces,[2] or most prominently simply by self-assembly.[11] The creation of paired QDs or even small arrays is possible for all the mentioned QD classes by a modified route for synthesis,,[6,7,9,12] in particular, in anisotropic self-assembling conditions for the lateral[13] or vertical[14] arrangement.

Along with the large manifold of synthesized QDs came a vast area of application of the tailor-made particles that build on the QD's discrete energy levels for electrons and holes. Two spectral ranges are particularly relevant. In the far- and mid-infrared range of intra-conduction band excitations of electrons (or valence-band excitations of holes) are addressed, which is used in infrared detection.[15] Ultraviolet and visible light (UV/Vis) allows for the crossing of the bandgap and the creation of excitons, which are subject to photo-catalysis,[16] quantum computing,[17,18] light-emission,[19–21] or solar cells functionality.[16,22]

The creation of a stable, *i.e.*, long-lived exciton is frequently discussed. Such stability would also play a key role in building block for quantum computers, since simple electron-hole recombination or the Auger process could easily destroy an exciton.[23] Furthermore, a stable exciton is of great importance in the creation of an electron-loaded QD surface to initiate chemical reaction.[24]

The key strategy behind this is hole trapping.[25,26] It relies on the relative energy levels of electron and hole of the QD and the embedding material. In a so-called type-II QD heterostructure a hole is favorably localized when both the valence-band maximum and the conduction-band minimum have higher energies than the embedding material, where, consequently, the electron would assemble.[25,26] Such charge separation leads ultimately to large permanent dipoles relevant to information storage[17] or solar cells.[22]

A promising material class in this respect is germanium QDs on a silicon surface.[25] Their optical structure is already well-investigated experimentally[27] and particular states can be addressed by lasers.[28,29] Such laser excitation scenarios were also found to be similarly successful in pairs of QDs.[14,30,31] Another strategy for electron and hole separation in pairs of QDs, or double quantum dots (DQDs), is potential-driven charge-carrier tunneling following photoexcitation.[32,33]

In this work, we would like to explore the exciton stabilization by hole trapping in combination with electron migration in self-assembled germanium DQDs. Specifically, by quantum-dynamical calculations we target a pump-dump process as shown in Fig. 1: UV radiation creates an exciton in the top Ge/Si nanocrystal, the exciton is then coherently transferred[34,35] to the lower QD, where it is eventually stabilized by subsequent IR de-excitation. We will show that the excitonic states involved in this two-pulse scheme consist of holes localized in the Ge structures and that the final stability will be obtained from localizing the electron.

Stability is always a matter of timescales, of course. Therefore, the lifetime of the exciton created should not exceed time spans on which decay processes in QDs may take place, namely Auger decay (1 ps),[36] acoustic phonon-mediated decay (50 ps $-$ 1 ns),[37,38] optical phonon-mediated decay (0.5 $-$ 5 ps),[37] or radiative recombination (1 ns).[36,39] Hence, the proposed three-step process is best investigated by an explicitly time-dependent method that includes a multitude of electronic states and that offers the possibility for the inclusion of decay mechanisms.

The theoretical modeling of nanostructures, however, is a challenge by itself and here two major routes are pursued. Either QDs are described by confinement models that can reflect the electronic band structures for geometries known from experiments.[40,41] Such models have

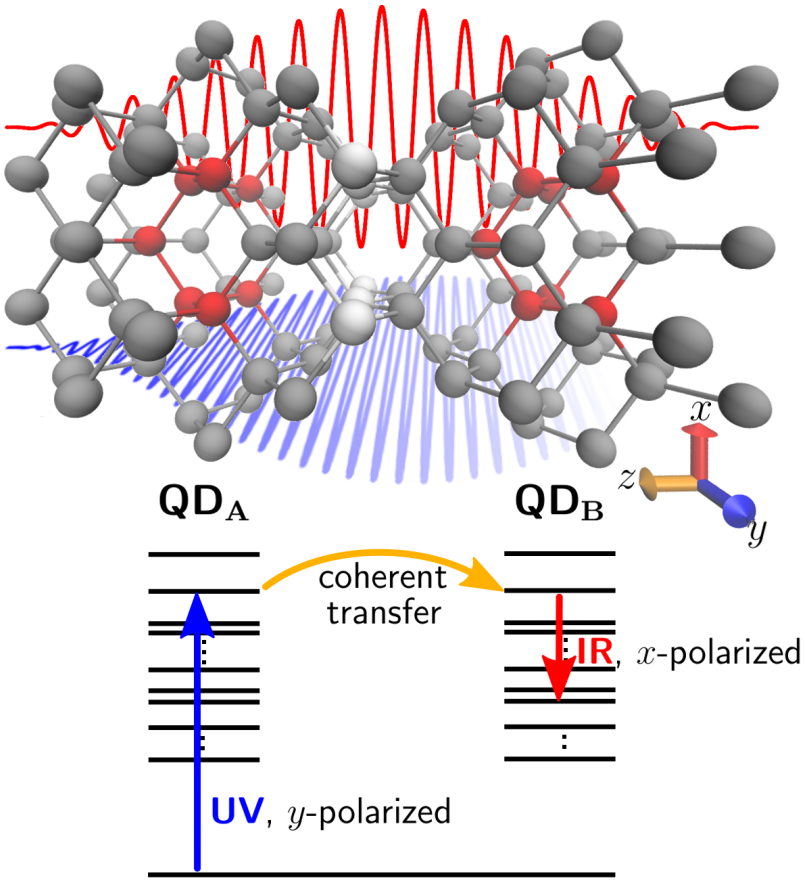

Figure 1: Top: Double QD made of Ge core nanocrystals (red spheres) embedded in Si shells (silver spheres). The core/shell Ge/Si nanocrystals are stacked along z direction (spacer layers are indicated by white spheres) and their absorption properties is schematically indicated by underlying laser pulses: $\mathrm{QD_B}$ is shielded from UV light excitation (fading blue lines) by Si layers while these layers are transparent for IR pulses (red lines). Bottom: schematic laser-control path by localized UV excitation, coherent transfer and IR fixation of specific hole-trapped state.

successfully been used to study Ge/Si structures[42–44] or electron dynamics in QD pairs.[38,39] In such models, though, the creation and annihilation of an exciton can only be accounted for indirectly. Hence, we follow the route based on an explicit atomistic description of the QDs. Experimental Ge/Si QDs exceed more than 100 atoms, which cannot be accurately treated in an all-electron description and reduced-size model QDs are employed. It was shown that small Ge clusters embedded in a few layers of Si shells do still feature the crucial optical properties of the original structures.[29,44,45]

For the study of light-induced electron dynamics, the time-dependent configuration interaction (TDCI) method that employs atom centered basis functions has proven to correctly describe the response properties of multi-electron polyatomic systems.[46–52] In the present work we study the laser-driven exciton dynamics in a double quantum dot made of a pair of Ge/Si model quantum dots. The excitonic properties and laser-induced electron-hole trapping in a single Ge/Si model QD was already successfully simulated at the time-dependent configuration interaction singles (TD-CIS) level of theory.[29] To better account for the electronic correlation, thereby offering a more accurate description of the electron dynamics, we adopt a hybrid time-dependent density functional theory/ configuration interaction (TDDFT/CI) formalism.[53–55] This yields a better energetic description of the systems' excited states at a numerical cost equivalent to the TD-CIS method. In our study we extend such single small molecular cluster models to build a double QD as depicted in Fig. 1 and introduce a dipole-dipole coupling between them. We present a UV+IR laser-driven pump-dump scheme where the delay time between the pulses depend on the transfer rate of the exciton between the two localized units of the DQD. This three-step process towards a stable exciton is schematically depicted in Fig. 1. We will show that the overall rate of the process is determined by the transfer time (orange arrow). This coherent transfer time, $\tau = h/2\Delta E$, is given by the energy splitting between intermediate excitonic states, which are representations of localized electron-hole pairs on single QDs obtained at the TDDFT level of theory and Coulomb coupled via dipole-dipole interaction.[56,57]

This paper is organized as follows: in section the theoretical background for the simulation

of laser-induced electron dynamics by the hybrid TDDFT/CI method is summarized and the establishment and construction of the Ge/Si model DQDs are elaborated. In section the results of the laser-controlled exciton dynamics are presented and discussed. Sec. summarizes the most significant results and gives an outlook on extending the model towards even more realistic representation. Atomic units ($e = \hbar = m_\mathrm{e} = 4\pi\varepsilon_0 = 1$) are used if not stated otherwise.

Theory

The evolution of a many-electron system driven by an external light source is governed by the electronic time-dependent Schrödinger equation (TDSE)

$$\mathrm{i}\frac{\partial|\Psi_\mathrm{el}(t)\rangle}{\partial t} = \hat{\mathbf{H}}(t)|\Psi_\mathrm{el}(t)\rangle \quad . \tag{1}$$

Here, $\hat{\mathbf{H}}(t) = \hat{\mathbf{H}}_\mathrm{el} + \hat{\mathbf{V}}^\mathrm{ext}(t)$ is explicitly time-dependent as it includes the electronic Hamiltonian, $\hat{\mathbf{H}}_\mathrm{el} = \hat{\mathbf{T}}_\mathrm{el} + \hat{\mathbf{V}}_\mathrm{el,el} + \hat{\mathbf{V}}_\mathrm{el,nuc}$, with its terms for kinetic and potential energy and the interaction with an oscillating external field, $\hat{\mathbf{V}}^\mathrm{ext}(t)$, *e.g.*, a laser pulse. Because the systems investigated here are relatively small in size compared to the excitation wavelength, coupling with an external electric field is treated in the semi-classical dipole approximation, $\hat{\mathbf{V}}^\mathrm{ext}(t) = \hat{\vec{\mu}}\cdot\vec{\mathrm{F}}(t)$. The molecular dipole operator for a system composed of i electrons and A nuclei is given by $\mu = -\sum_i^N r_i + \sum_A^{N_A} Z_A R_A$. Provided that the electronic wavefunction, $|\Psi_\mathrm{el}(t)\rangle$, at a given initial time, t_0, is known, the wavefunction at any time, t, can be computed by integrating Eq. 1.

For the description of exciton dynamics in many-electron systems, correlated wavefunction methods provide a potentially powerful approach. In this context, the configuration interaction (CI) methodology represents a straightforward and systematic way to include electron correlation in the many-body wavefunctions. In its single-reference version, dynamic correlation is included by creating excited configurations from a reference Slater determinant of the ground state. This is done by systematically promoting one or more electrons from occupied orbitals $\mathrm{a}, \mathrm{b}, \mathrm{c}, \ldots$ of that determinant to unoccupied orbital $\mathrm{r}, \mathrm{s}, \mathrm{t}, \ldots$. By symmetrizing the spin of these excited

configurations, so-called configuration state functions (CSFs) are constructed.

Since optical processes predominantly involve the excitation of a single electron in the space of correlated virtual orbitals,[58] taking only singly excitations into account is common place when treating electron dynamics on a femtosecond timescale. This leads to so-called the CI single method, where the many-electron wavefunction in Eq. 1 is approximated by its CIS counterpart, $|\Psi^{\mathrm{el}}(t)\rangle \approx |\Psi^{\mathrm{CIS}}(t)\rangle$. However, at the CIS level of theory the ground state remains the uncorrelated Hartree-Fock state and excitation energies are often too large.[58] Density functional theory (DFT) in its Kohn-Sham formulation offers a solution to this problem by including explicitly electron correlation into the ground state Slater determinant.[59]

Time-dependent hybrid-TDDFT/CI

For the solution of Eq. 1, the time-dependent wavefunction is expanded in a basis of pseudo-CIS eigenstates, $|\Psi_i^{\mathrm{CIS}}\rangle$

$$|\Psi_{\mathrm{el}}\rangle(t) \approx \sum_i C_i(t)|\Psi_i^{\mathrm{CIS}}\rangle \quad , \tag{2}$$

where the expansion coefficients at any given time, $C_i(t)$, are obtained by direct numerical integration. The pseudo-CIS eigenstates are themselves written as truncated CI expansions,

$$|\Psi_i^{\mathrm{CIS}}\rangle = \delta_{i0}|\Psi_0\rangle + \sum_{\mathrm{ar}}(1-\delta_{i0})D^{\mathrm{r}}_{\mathrm{a},(i)}|\Psi^{\mathrm{r}}_{\mathrm{a}}\rangle, \tag{3}$$

where the indices imply sums over all occupied spin orbitals, $\{\mathrm{a}\}$, all unoccupied spin orbitals, $\{\mathrm{r}\}$ and the Kronecker delta is used as a coefficient for the ground state Kohn-Sham determinant $|\Psi_0\rangle$. To improve on the system energetics while retaining the simple form of the CIS wavefunctions, the coefficients $D^{\mathrm{r}}_{\mathrm{a},(i)}$ are computed using linear-response time-dependent density functional theory (LR-TDDFT).[54,59] Within the Tamm-Dancoff approximation, the equivalence between the LR-TDDFT pseudo-eigenfunctions, $|\Psi_i^{\mathrm{TDDFT}}\rangle$, and the CIS expansion, $|\Psi_i^{\mathrm{CIS}}\rangle$, is strict, when the former uses a Kohn-Sham ground state as a single reference. The method is also known as time-dependent Tamm-Dancoff approximation (*TD-TDA*).[55] By choosing an appropriate exchange-

correlation functional, some of the electron correlation is included in the Kohn-Sham orbitals of the ground state reference determinant, $|\Psi_0\rangle$. This improves the energies of the orbitals and provides a more accurate bandgap than in canonical Hartree-Fock orbitals, which serves as a starting point for the standard CIS procedure. Ultimately, this leads to more accurate energies for the excited many-electron pseudo-CIS eigenstates.

Keeping only the contributions larger than some user-defined threshold, $|D^{\mathrm{r}}_{\mathrm{a},(i)}| > \varepsilon$, a compact representation of the pseudo-CIS eigenfunction is obtained. Renormalization of the selected response coefficients associated with each pseudo-CIS eigenstates yields approximate CIS wavefunctions of the form Eq. 3, which can be used to compute the matrix elements of the time-dependent Hamiltonian in Eq. 1. The TDCI method needs excitation energies and the corresponding dipole matrix only to allow performing laser-driven electron dynamics.[48]

The pseudo-CIS eigenvectors are further used to calculate the elements of the transition dipole moment matrices along the three Cartesian directions q are calculated from the CIS eigenvectors as

$$\mu_{ij;q} = \langle \Psi_i^{\mathrm{CIS}} | \hat{\mu}_q | \Psi_j^{\mathrm{CIS}} \rangle \quad . \tag{4}$$

The diagonal elements $i = j$ represent the permanent dipole of a given state, and the off-diagonal elements the transition dipole moments which mediate optical transitions between states i and j.

Furthermore, for the analysis and characterization of the electronic transitions, natural transition orbitals (NTO)[60] are constructed. The multi-determinantal excited state wavefunctions in NTOs are expressed through a one-electron transition density matrix between this reference $|\Psi_{\mathrm{ref}}\rangle$ and the excited state. By this compact representations a qualitative description of an electronic transition of the correlated pairs of particle and hole functions can obtained. All integrals can be computed analytically from the knowledge of the pseudo-CIS wavefunctions, see below for computational details. Finally, propagation of the expansion coefficients of the time-dependent

wavefunction is done by direct numerical integration of the linearized equations of motion, using an in-house code described in detail elsewhere.[53,54,56,61]

Exciton model

To simulate the dynamics in a pair of interacting quantum dots, we build upon the knowledge of the pseudo-CIS wavefunctions and construct a Frenkel exciton model.[62–64] In the present context, the dynamics describes the time-evolution of non-covalently interacting stacked QDs, and the choice of Frenkel exciton model appears natural, as it is amenable to the description of large arrays of interacting QDs. The basic idea is to represent an excitonic state as a direct product of electronic states of individual QDs, here labelled $\mathrm{QD_A}$ and $\mathrm{QD_B}$: $|\Psi^{\mathrm{CIS}}_{n_\mathrm{A}}\rangle \otimes |\Psi^{\mathrm{CIS}}_{n_\mathrm{B}}\rangle$. By using such product ansatz, excitonic states in the double quantum dots are generated, in which independent electron-hole pairs are localized on individual QDs, and the transfer of an electron from one QD to the other is not possible. These required building blocks – the local electron-hole pair wavefunctions – are constructed by combining results of the single point calculations in the individual QDs.

The zeroth-order energy of the excitonic states are simply given as the sum of energies of the individual QD fragments. By construction, these excitonic states can be separated energetically in two excitation bands. The first mixes excited states of one quantum dot while the other remains in the ground state ($|\Psi^{\mathrm{CIS}}_{0_\mathrm{A}}\rangle \otimes |\Psi^{\mathrm{CIS}}_{n_\mathrm{B}}\rangle$ and $|\Psi^{\mathrm{CIS}}_{n_\mathrm{A}}\rangle \otimes |\Psi^{\mathrm{CIS}}_{0_\mathrm{B}}\rangle$). The second band is made of all combinations of excitation in both clusters, and it is located at about twice the energy of the first band. To rule out multi-photon effects when inducing a transitions to low-lying exciton states, basis for propagations is truncated to the first band. This leads to a Frenkel exciton wavefunction of the form

$$|\Psi(t)\rangle \;=\; \sum_{n_\mathrm{A}} c_{n_\mathrm{A}0_\mathrm{B}}(t)|\Psi^{\mathrm{CIS}}_{n_\mathrm{A}}\rangle \otimes |\Psi^{\mathrm{CIS}}_{0_\mathrm{B}}\rangle + \sum_{n_\mathrm{B}} c_{0_\mathrm{A}n_\mathrm{B}}(t)|\Psi^{\mathrm{CIS}}_{0_\mathrm{A}}\rangle \otimes |\Psi^{\mathrm{CIS}}_{n_\mathrm{B}}\rangle \quad . \tag{5}$$

The total Hamiltonian of the two interacting QDs in Eq. 1 can be approximated by the Frenkel

Hamiltonian of the excitonic system as

$$\begin{aligned}\hat{\mathbf{H}} &= \sum_{n_\mathrm{A}} \varepsilon_{n_\mathrm{A}} |\Psi^{\mathrm{CIS}}_{n_\mathrm{A}}\rangle\langle\Psi^{\mathrm{CIS}}_{n_\mathrm{A}}| \otimes \hat{\mathbf{I}}_\mathrm{B} + \sum_{n_\mathrm{B}} \hat{\mathbf{I}}_\mathrm{A} \otimes \varepsilon_{n_\mathrm{B}} |\Psi^{\mathrm{CIS}}_{n_\mathrm{B}}\rangle\langle\Psi^{\mathrm{CIS}}_{n_\mathrm{B}}| \\ &+ \sum_{\substack{n_\mathrm{A} n_\mathrm{B} \\ m_\mathrm{A} m_\mathrm{B}}} V^{\mathrm{dd}}_{\substack{n_\mathrm{A} n_\mathrm{B} \\ m_\mathrm{A} m_\mathrm{B}}} |\Psi^{\mathrm{CIS}}_{n_\mathrm{A}}\rangle\langle\Psi^{\mathrm{CIS}}_{m_\mathrm{A}}| \otimes |\Psi^{\mathrm{CIS}}_{n_\mathrm{B}}\rangle\langle\Psi^{\mathrm{CIS}}_{m_\mathrm{B}}| \quad . \end{aligned} \tag{6}$$

The Coulomb interaction between the two stacked QDs is approximated as the coupling of two dipoles, as found in the non-radiative Förster resonance energy transfer:[65]

$$\hat{\mathbf{V}}^{\mathrm{dd}} = \kappa \frac{|\vec{\mu}_\mathrm{A}|\,|\vec{\mu}_\mathrm{B}|}{\mathrm{R}_0^3} \quad , \tag{7}$$

where R_0 is the distance between the centers of the QDs. The orientation factor

$$\kappa = \frac{\vec{\mu}_\mathrm{A} \cdot \vec{\mu}_\mathrm{B}}{|\vec{\mu}_\mathrm{A}|\,|\vec{\mu}_\mathrm{B}|} - 3\frac{\left(\vec{\mu}_\mathrm{A} \cdot \vec{R}\right)\left(\vec{\mu}_\mathrm{B} \cdot \vec{R}\right)}{|\vec{\mu}_\mathrm{A}|\,|\vec{\mu}_\mathrm{B}|\,R_0^2} \tag{8}$$

depends on the displacement vector $\vec{R}$ between the two QDs. This particular shape of the operator simplifies evaluation of the coupling term in the excitonic basis as

$$\begin{aligned} V^{\mathrm{dd}}_{\substack{n_\mathrm{A} n_\mathrm{B} \\ m_\mathrm{A} m_\mathrm{B}}} &= \langle\Psi^{\mathrm{CIS}}_{n_\mathrm{A}}|\langle\Psi^{\mathrm{CIS}}_{n_\mathrm{B}}|\hat{\mathbf{V}}^{\mathrm{dd}}|\Psi^{\mathrm{CIS}}_{m_\mathrm{B}}\rangle|\Psi^{\mathrm{CIS}}_{m_\mathrm{A}}\rangle \\ &= \frac{\kappa}{R_0^3} \left|\langle\Psi^{\mathrm{CIS}}_{n_\mathrm{A}}|\vec{\mu}_\mathrm{A}|\Psi^{\mathrm{CIS}}_{m_\mathrm{A}}\rangle\right| \left|\langle\Psi^{\mathrm{CIS}}_{n_\mathrm{B}}|\vec{\mu}_\mathrm{B}|\Psi^{\mathrm{CIS}}_{m_\mathrm{B}}\rangle\right| \quad . \end{aligned} \tag{9}$$

The required transition dipole moments are calculated from the pseudo-CIS eigenfunctions obtained from a single point calculation of the individual QDs, Eq. 4. The eigenvectors and eigenenergies necessary to perform the TDCI dynamical simulations and integrate numerically Eq. 1 are obtained by diagonalizing the matrix representation of the Hamilton Operator in the Frenkel exciton basis

$$\begin{aligned} &\mathbf{HU} = \mathbf{UE} \\ &|\Psi_i\rangle = \sum_{m_\mathrm{A}, m_\mathrm{B}} U_{\{m_\mathrm{A}, m_\mathrm{B}\}, i} |\Psi^{\mathrm{CIS}}_{m_\mathrm{A}}\rangle \otimes |\Psi^{\mathrm{CIS}}_{m_\mathrm{B}}\rangle \quad . \end{aligned} \tag{10}$$

The similarity transformation allows to define a rotation matrix $\mathbf{U}$ with elements $U_{\{m_\mathrm{A},m_\mathrm{B}\},i}$ which relates the localized Frenkel exciton states $|\Psi^{\mathrm{CIS}}_{m_\mathrm{A}}\rangle \otimes |\Psi^{\mathrm{CIS}}_{m_\mathrm{B}}\rangle$ to the delocalized eigenstates $|\Psi_i\rangle$. The effect of this transformation is shown in Fig. 2. On the left, the energy levels of

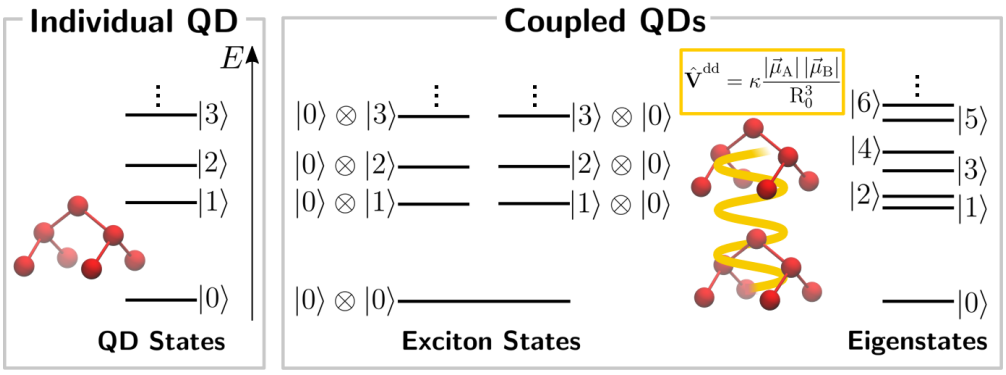

Figure 2: Schematic energy levels of the Ge/Si clusters for the individual QD (left) and the double QD (right); distinction of exciton and eigenstates.

the individual QDs, computed here using LR-TDDFT in the Tamm-Dancoff approximation, are shown. The Frenkel excitonic states are depicted in the center, with the ground state remaining completely delocalized. This basis will be later used to analyze the dynamics in terms of localized excitations. The coherent coupling between the two QDs is represented as a wavy orange arrow. Note that only the germanium atoms (red spheres) are depicted to simplify the representation, but all clusters include a double silicon shell saturated by hydrogen atoms, as depicted in Fig. 1. On the right, the basis of delocalized eigenstates of the Frenkel Hamiltonian used in the TDCI simulations is shown. The unitary transformation matrix $\mathbf{U}$ allows to toggle back and forth between the TDCI propagation basis and the excitonic basis.

The Coulomb interaction between individual QD dipoles gives rise to an energy splitting that is a function of separation of the QDs. The magnitude of this energy splitting depends on both the change of permanent dipole moments of the states and the transition dipole moments among them. It is found to be small and involves mostly coupling of excitonic states with the same electron-hole pair character on either of the QDs. The coherent nature of this interaction is reflected in the transfer between excitonic states localized on each QD. For every pair of coupled localized excitonic states, the rate associated with this coherent transfer depends on the energy

difference ΔE between eigenstates with a similar local electron-hole pair character on each QD.

The present work reports on the scenario where two self-assembled QDs are stacked on top of each other. This situation is represented in Fig. 1, where the z axis corresponds to the the orientation normal to the silicon wetting layer on which germanium atom grow. The double QD system is excited using an electric field polarized in the xy-plane and propagating towards the positive z direction. The germanium cluster $\mathrm{QD_B}$ is buried below $\mathrm{QD_A}$. Because the electric field will cross a thicker layer of silicon to reach the second QD deeper inside the silicon surface, the electric field will be more efficiently screened by the silicon wetting layer, depending on the frequency of the incoming laser pulse. Silicon becomes opaque for excitation energies larger than $E_{\mathrm{cutoff}} = 1.2\,\mathrm{eV}$.[66,67] This implies that UV laser excitations will likely interact with the top cluster only. However, both clusters are still sensitive to IR excitation, which lies in a frequency domain for which silicon is almost transparent. To represent this situation, which is schematically depicted in Fig. 1, the dipole moment matrix used to evaluate the coupling of the individual QDs with the external field is modified. An effective dipole matrix, $\tilde{\boldsymbol{\mu}}_{\mathrm{eff}}$ is defined such that all components representing a transition at an energy $\Delta E_{\mathrm{n_B}} > E_{\mathrm{cutoff}}$ for the $\mathrm{QD_B}$ at the bottom is set to zero in the exciton basis. That way, coupled quantum dots in a symmetric donor-acceptor configuration are constructed. For the propagation in the eigenstate basis, the effective dipole matrix is then transformed using the same unitary transformation as described above, $\boldsymbol{\mu}_{\mathrm{eff}} = \mathbf{U}^t \tilde{\boldsymbol{\mu}}_{\mathrm{eff}} \mathbf{U}$. Therefore, the effective interaction Hamiltonian used for the laser-induced dynamics in the time-dependent calculations includes the different absorption properties in the UV regime for the two QDs.

Laser field design

To drive the dynamics, we apply a series of $\cos^2$-shaped laser pulses which are chosen to be

$$\vec{F}(t) = \sum_n \vec{f}_n(t) \cos\left[\omega_n(t - t_{p,n}) + \Phi_n\right] \text{ with,} \tag{11}$$

$$\vec{f}_n(t) = \begin{cases} \vec{f}_{0,n} \cos^2\left[\frac{\pi}{2\sigma_n}(t - t_{p,n})\right] & \text{if } \mid t - t_{p,n} \mid < \sigma_n \\ \vec{0} & \text{else} \quad , \end{cases} \tag{12}$$

where the index $n = 1, 2$ indicates the number of the laser pulse. The polarization and the maximum amplitude, which is reached at $t_{p,n}$, is given by $\vec{f}_{0,n}$. The frequency is ω_n, while σ_n and Φ_n determine the full width at half maximum (FWHM) and the phase of the nth laser pulse.

In the results section we will present laser excitations that induce a population inversion. Such inversions between Ψ_m and Ψ_n can be achieved using so-called π-pulses, derived from Rabi oscillations in a driven two-level system within the rotating wave approximation. The field amplitude and pulse duration for the individual $\cos^2$-shaped pulses can be explicitly calculated from the following condition

$$|\vec{f}_0| \cdot \sigma = \pi / |\vec{\mu}_{i,j}| \quad , \tag{13}$$

for collinear vectors $\vec{f}_0$ and $\vec{\mu}_{i,j}$, as defined in Eq. 4. The associated maximum field intensities are calculated as

$$I_\mathrm{max} = \frac{1}{2} \varepsilon_0 \, \mathrm{c} \, \vec{f}_0^{\,2} \quad , \tag{14}$$

where ε_0 is the vacuum permittivity and c is the velocity of light. Note, that the rotating wave approximation and the assumption of an ideal two-level system are only used for the determination of the initial laser pulse parameters. All dynamics simulations presented later have been carried out using a manifold of electronic states.

Model and Methods

We present simulations on three Ge/Si core/shell nanocrystals that differ in size and geometry. Their main structure element is a QD core of covalently bound germanium atoms, namely either a pyramidal Ge_7 (depicted in Fig. 2) or two isomeric Ge_{11} cores assigned as HAT-A and HAT-B. The silicon atoms form the diamond-structured host matrix in such a way that each Ge atom has got two layers of nearest neighbors of Si atoms. Any dangling bonds of the outer Si shell are passivated with hydrogen atoms.

To impose the diamond lattice of bulk Si, all geometry optimizations are carried out while freezing the second layer of Si atoms. That way C_{2v} symmetry is imposed to the clusters during geometry optimization at PBE/def2-SVP level of theory[68,69] employing the *TURBOLMOLE* package.[70] The lowest-lying 50 electronic states are taken from subsequent single-point LR-TDDFT calculations in the Tamm-Dancoff approximation employing the PBE0/def2-SVP functional to build electronic states of the exciton model. All single-point electronic structure calculations are performed using the *ORCA* code.[71]

These single molecular clusters models are taken to build a double QD as depicted in Fig. 1 and introduce a dipole-dipole coupling between them (orange arrow). All 50 electronic states are used for the construction of the 2500 exciton states Eq. 5 of the double dot. By subsequent diagonalization of the effective interaction Hamiltonian the exciton state functions and the corresponding dipole matrix are obtained. Propagations are carried out with the first 99 states that form the first exciton band as described in .

The coefficients of the pseudo-CIS eigenstates are pruned at a cutoff threshold of $|D^i_{\mathrm{a}}| > \varepsilon$, with $\varepsilon = 0.01$ (see section). The transition dipole moments from the corresponding pseudo-CIS eigenvectors are computed using the module DETCI of the open-source post-processing program ORBKIT.[54,72,73] Note, that the sign of all transition dipole moment elements from the ground state, Eq. 4, have been set to positive values to ensure a systematic sign convention. This is possible since each pseudo-CIS eigenstate obtained from LR-TDDFT is defined up to a global absolute phase, without any relation among them. These phases are determined numerically and

have no physical meaning. Yet, the phases have an important influence on the construction of the exciton Hamiltonian, see Eq. 9. Finally, propagation of the expansion coefficients of the time-dependent wavefunction is done using an in-house code described in detail elsewhere.[29,53,54,56,57] Here, direct numerical integration of the linearized equations of motion is performed using as a preconditioned adaptive step-size Runge-Kutta algorithm.[74]

Results and Discussion

The pyramidal Ge_7/Si core/shell double QD

For the study of the exciton transfer in different double quantum dots we discuss first the pair of the smallest nanocrystals of our series, the pyramidal Ge_7 core structures. We present a laser-driven pump-dump scheme where the delay time between the pulses is tuned according to the transfer rate between excitonic states. This three-step process towards a stable exciton is schematically depicted in Fig. 1. Since the stacked QDs are constructed by combining results of individual QDs, a distance has to be determined in order to A) obtain a "large" energy splitting between eigenstates for intermediate states and B) low-lying states with a vanishing splitting between the final electron-hole pair states. Since the Coulombic coupling is weak at larger distances, a single spacer layer that matches the diamond lattice of Si bulk was sufficient.

Although the calculations of the dynamics are performed in the eigenstate basis of the QD pair, discussion of results is better visualized in terms of the corresponding localized Frenkel excitonic states, cf. Fig. 2. It is more intuitive since the distinction between top and bottom cluster is clearer and the exciton exchange is directly visible. Therefore, the excitation path in the exciton basis reads for example: $|0\rangle \otimes |0\rangle \overset{\mathrm{UV}}{\longrightarrow} |14\rangle \otimes |0\rangle \overset{transfer}{\longrightarrow} |0\rangle \otimes |14\rangle \overset{\mathrm{IR}}{\longrightarrow} |0\rangle \otimes |6\rangle$. However, an exciton population of the first step of $P(|14\rangle \otimes |0\rangle) = 1$ and $P(|0\rangle \otimes |14\rangle) = 0$ results in the localized excitation on the top QD and is actually the result of a coherent eigenstate population of $P(|27\rangle) = 0.5$ and $P(|28\rangle) = 0.5$. Hence, the above mentioned targeted excitation path is a result of the linear combination of pairs of eigenstates and the actual propagation pathway reads:

$|0\rangle \xrightarrow{UV} |27\rangle/|28\rangle \xrightarrow{IR} |11\rangle/|12\rangle$.

Careful selection of intermediate and target state properties largely supports the exciton transfer-mediated hole trapping. In addition to these energetic constrains that intermediate states have a large energy splitting and target states have a vanishing energy difference, they need to be accompanied by pairwise sufficiently large transition dipole elements to be accessible by radiation at moderate intensities. The selected pairs of eigenstates that fulfill such conditions are listed in Tab. 1, which shows the excitonic composition of the eigenstates of the coupled QDs. Tab. 2 lists their energies and dipole moments. In Tab. 2 is seen that the target eigenstates $|11\rangle$ and $|12\rangle$ have a very small ΔE, while it is much larger for the intermediate pair states $|27\rangle$ and $|28\rangle$.

Table 1: Eigenstates and their contributions $|n_{\mathbf{A}}\rangle \otimes |n_{\mathbf{B}}\rangle$ from excitonic states for the pyramidal Ge_7 core structure. The contributions of each excitonic state is given in parentheses.

Eigenstate	Exciton State (Contribution)
$\|11\rangle$	$\|6\rangle \otimes \|0\rangle$ $(c = +0.7018)$ $\|0\rangle \otimes \|6\rangle$ $(c = -0.7123)$
$\|12\rangle$	$\|6\rangle \otimes \|0\rangle$ $(c = +0.7123)$ $\|0\rangle \otimes \|6\rangle$ $(c = +0.7018)$
$\|27\rangle$	$\|14\rangle \otimes \|0\rangle$ $(c = -0.7063)$ $\|16\rangle \otimes \|0\rangle$ $(c = +0.0323)$ $\|0\rangle \otimes \|14\rangle$ $(c = -0.7063)$ $\|0\rangle \otimes \|16\rangle$ $(c = +0.0323)$
$\|28\rangle$	$\|14\rangle \otimes \|0\rangle$ $(c = -0.7064)$ $\|16\rangle \otimes \|0\rangle$ $(c = +0.0303)$ $\|0\rangle \otimes \|14\rangle$ $(c = +0.7064)$ $\|0\rangle \otimes \|16\rangle$ $(c = -0.0303)$

The exciton contributions given in Tab. 1 show that the target states $|11\rangle$ and $|12\rangle$ are composed solely from excitation to the sixth local excited state on either of the QDs, *i.e.*, from the excitonic states $|0\rangle \otimes |6\rangle$ and $|6\rangle \otimes |0\rangle$, respectively, while the intermediate eigenstates $|27\rangle$ and $|28\rangle$ have mixed excitonic contributions involving the excitations $|14\rangle$ and $|16\rangle$ on either of the dots. Although excitonic state $|16\rangle \otimes |0\rangle$, for example, has a rather small contribution, its transition dipole moment may be neglected in the design of the laser pulse.

The corresponding dipole matrix with its Cartesian components is shown in the upper triangle of Tab. 2. The permanent dipole moments of the states are given on the diagonal, while the off-diagonal elements of the matrix are the transition dipole moments. Those values that are highlighted in orange are responsible for the amount of energy splitting between pairs of eigenstates $|11\rangle/|12\rangle$ and $|27\rangle/|28\rangle$. The magnitude of the transition dipoles, however, determines the possible relations for laser amplitude and duration for the π-pulses (cf. Eq. 13). Highlighted in blue and red are the transition dipole elements that are used for the UV and IR excitation in the simulations. For the first UV pulse excitation, for example, $|0\rangle \overset{UV}{\longrightarrow} |27\rangle/|28\rangle$, Tab. 2 shows that a laser polarization along the y direction mediates the transition. However, by the construction of a donor-acceptor DQD sytem, only the top cluster is receptive for UV radiation. Therefore, the transition dipole moments of state $|27\rangle$ and $|28\rangle$ are scaled by their excitonic contribution of $|14\rangle \otimes |0\rangle$ as $0.129\ \mathrm{ea_0}/0.7063 = 0.183\ \mathrm{ea_0}$, cf. Tab. 1 and Tab. 2 (which in the end corresponds to the transition dipole moment $\mu_{0,14}$ of the single QD). Later, an x polarized IR pulse dumps the

Table 2: The upper triangle shows the Cartesian components of the dipole matrix of selected eigenstates given in $\mathrm{ea_0}$. In the lower triangle the energy differences between these states are given in eV. Highlighted in blue and red are the transition dipole moments and frequencies used for UV and IR π-pulse excitation, respectively. Highlighted in orange are the permanent dipole moments of the eigenstates that drive the transfer and hole trapping dynamics.

	$\|0\rangle$	$\|11\rangle$	$\|12\rangle$	$\|27\rangle$	$\|28\rangle$
$\|0\rangle$	$\begin{pmatrix} -0.000 \\ +0.000 \\ -0.496 \end{pmatrix}$	$\begin{pmatrix} +0.000 \\ -0.000 \\ -0.003 \end{pmatrix}$	$\begin{pmatrix} +0.000 \\ -0.000 \\ +0.355 \end{pmatrix}$	$\begin{pmatrix} -0.000 \\ -0.129 \\ -0.327 \end{pmatrix}$	$\begin{pmatrix} -0.000 \\ -0.127 \\ -0.000 \end{pmatrix}$
$\|11\rangle$	3.8531	$\begin{pmatrix} +0.000 \\ +0.000 \\ -2.154 \end{pmatrix}$	$\begin{pmatrix} +0.000 \\ +0.000 \\ +0.000 \end{pmatrix}$	$\begin{pmatrix} -0.007 \\ -0.093 \\ -0.002 \end{pmatrix}$	$\begin{pmatrix} +0.870 \\ -0.092 \\ +0.236 \end{pmatrix}$
$\|12\rangle$	3.8531	$3.0211 \cdot 10^{-14}$	$\begin{pmatrix} +0.000 \\ -0.000 \\ -2.154 \end{pmatrix}$	$\begin{pmatrix} +0.877 \\ +0.092 \\ +0.234 \end{pmatrix}$	$\begin{pmatrix} +0.007 \\ +0.091 \\ +0.002 \end{pmatrix}$
$\|27\rangle$	4.0071	0.1541	0.1541	$\begin{pmatrix} -0.000 \\ -0.171 \\ -0.331 \end{pmatrix}$	$\begin{pmatrix} +0.000 \\ +0.002 \\ +0.000 \end{pmatrix}$
$\|28\rangle$	4.0075	0.1545	0.1545	$4.0165 \cdot 10^{-4}$	$\begin{pmatrix} -0.000 \\ +0.169 \\ -0.330 \end{pmatrix}$

excitonic population from high excited states to low-lying target states, $|27\rangle/|28\rangle \xrightarrow{\mathrm{IR}} |11\rangle/|12\rangle$, which terminates the exciton exchange process.

For the dynamics, our knowledge on the system regarding excitation energies and dipole moments allows to target the process through careful laser design. Laser parameters for both the UV pump and the IR dump pulse are chosen in the following manner: to mimic the fact that the Ge/Si DQDs grow on top of the silicon surface, laser polarizations are perpendicular to the stacking direction while the field propagates into the surface. By doing so, non-linear coupling of laser field and electronic states can be reduced, since the permanent dipoles of the clusters are large along this stacking direction. For the exciton transfer it is necessary to induce a population inversion preferably at each excitation step. Therefore, simple π-pulses (Eq. 13) with cosine squared envelope are used to determine the relation between maximum field strength f_0 and pulse duration 2σ.

A priori theoretical analysis of the eigenstates properties allows to identify a promising excitation scheme through intermediate states with a short transfer time, together with an estimate of the required laser parameters. Fine-tuning of the lasing action is done through parametric optimization of the laser strength and pulse duration of both the UV and the IR pulse, as well as the pump-dump delay time. The laser pulse strength is first obtained from Eq. 13 for π-pulses of 500 fs and 1 ps duration in the UV and IR case, respectively. These pulse durations are short enough to avoid vibration-induced relaxation in such rigid systems and long enough to prevent dynamical broadening. At least in the specific case of GeSi, phonon lifetimes were found to be on the order of a few ps and longer.[29] The π-pulse durations are then optimized to obtain a maximal population inversion for each excitation step.

The resulting laser-driven population dynamics can be viewed in Fig. 3. The upper panel shows the dynamics in terms of eigenstate populations, whereas the lower panel shows the respective excitonic state population evolution. In the eigenstate basis (upper panel), the first pulse is resonant with the $|27\rangle \leftarrow |0\rangle$ transition at an excitation energy of 4007 meV. It is polarized along the y direction and drives a transition from the ground state (purple curve) to coherent

superposition of states $|27\rangle$ and $|28\rangle$ (blue and light blue) with an almost equal population of 0.507 and 0.485.

The magnitude of the transition dipole moments along the y direction allows using a moderate laser intensity of $I_{\max} = 102$ GW/cm^2 with a duration of $2\sigma_1 = 483.8$ fs. The second transition is driven by a x-polarized re-optimized π-pulse resonant with $|12\rangle \leftarrow |28\rangle$ (154 meV), at a much lower intensity of $I_{\max} = 0.732$ GW/cm^2 due to the longer duration of $2\sigma_2 = 1209.44$ fs. The final populations in the target states $|12\rangle/|11\rangle$ are $0.0.495/0.463$.

For a more straightforward and intuitive view of the excitation and charge separation process studied here, the dynamics is additionally presented in the exciton basis in the bottom panel of Fig. 3. After UV pulse excitation, the population of the excitonic state $|14\rangle \otimes |0\rangle$, in which the topmost quantum dot is excited while the other remains in its ground state, reaches a maximum of 0.985 after 0.435 ps. Note that the total population of states $|27\rangle$ and $|28\rangle$ is larger than the population of the target excitonic state after the excitation. This is because each excited eigenstate contains small components in other excitonic states, which bear the remainder of the population. The ground state population drops to 0.007 in that time where it remains until the end of propagation. Coherent exchange between states $|14\rangle \otimes |0\rangle$ and $|0\rangle \otimes |14\rangle$ (dashed blue and light blue curves) takes place right after the start of the UV pulse, however, it is much slower than the laser-induced change of occupation. Within 4.5 ps the exciton is thus transferred from the top to the bottom quantum dot, an effect that was hidden in the eigenstate representation. The IR pulse sets in shortly before the end of the formal transfer exchange. With the center of the IR dump pulse at $t_{p,2} = 5.44$ ps, a maximal population of the target state $|0\rangle \otimes |6\rangle$ (red lines) of 0.954 is achieved. In this state only the bottom Ge_7 cluster bears an exciton. The corresponding excitation on the upper cluster, $|6\rangle \otimes |0\rangle$ (orange line), is with 0.001 barely populated. Due to the very small energy difference between these states, even after 50 ps no exciton transfer can be observed, as seen in the inset. That means, a stable exciton state is created in the bottom cluster, QD_B. During the full pump-dump cycle some transient populations to various excited states occur (black curves in both panels), however, they are not relevant for the overall population dynamics.

The character of the laser-induced transition can be evaluated using natural transition orbitals. Hole-trapping in the topmost quantum dot is observed in the first excitation step already – as seen in the NTO densities of exciton state $|14\rangle$ from the calculation of the single QD in the top of Fig. 4. The hole densities, represented by grey isosurfaces, show a fairly localized hole in the pyramidal Ge_7 structure. In contrast, the NTO density of the electron (blue isosurfaces) is spread throughout the silicon shells. The IR pulse changes the distribution of the hole density only a little by centering it even further to the Ge structure, as its NTO density in the bottom figure shows. But importantly, it strongly localizes the electron in the Si bulk right below the Ge cluster. Note that the NTO densities do not only explain the charge separation, but, in direct relation, also the magnitude of the permanent dipole moments of the considered eigenstates. In the final charge-separated exciton $|0\rangle \otimes |6\rangle$, the permanent dipole is large along the z direction, $-2.15\ \mathrm{ea_0}$ (*cf.* the values for eigenstates $|11\rangle$ and $|12\rangle$ in Tab. 2). With $-0.33\ \mathrm{ea_0}$ along the z direction, it is much smaller for the intermediate ones $|27\rangle$ and $|28\rangle$, where it is also much less directed along the DQD stacking direction having a non-negligible contribution of $\pm 0.17\ ea_0$ also along y.

Summarizing, from investigation of two pyramidal Ge clusters in a Si shell, we can deduce that a combined UV-IR pump-dump excitation scheme can selectively create a stable, charge-separated state on an acceptor quantum dots that is otherwise not accessible using a single pulse alone.

The Ge_{11}/Si double QDs

The following section explores the transferability of the aforementioned excitation scheme on two slightly larger symmetric double dot. These nanocrystals both have Ge_{11} cores of different geometry, which will be addressed as HAT-A and HAT-B. The single QD structures can be viewed in the top left panels of Fig. 5 and Fig. 6, respectively, along with the NTO densities associated with the intermediate (top) and final (bottom) states. In both cores, the Ge_7 core from the pyramidal cluster is extended along the x direction, and the structures differ only in their connectivity with the first silicon shell. Including the hydrogen atoms that saturate the

second silicon shell, chosen to retain the structure of the diamond lattice, the two nanocrystals possess 161 and 162 atoms in total. For the excitonic system, symmetric DQDs are constructed by stacking these single clusters along the z direction, as described in the previous sections. The larger Ge_{11} clusters both have a higher density of states compared to Ge_7. This is reflected in the larger amount of excitonic states involved in the composition of the eigenstates of the DQDs. The dominant contributions for the intermediate and final states to be used in the pump-dump dynamics are shown in tables in the center of Fig. 5 and Fig. 6 for HAT-A and HAT-B, respectively.

Compared to the DQD of the pyramidal Ge_7 structure, however, important similarities in the nature of the excited states can be found. This enables to design a very similar pump-dump scheme in the larger DQDs, using UV and IR pulse excitations with x and y polarizations. For both Ge_{11} cores, states with energy splittings that are large for intermediate and small for the target states are readily found as well. The final states also exhibit a similar degree of hole localization, as revealed by the NTO analysis (see left panels in Figs. 5 and 6), such as to allow efficient laser-driven hole trapping. The selected intermediate and final states are accompanied by transition dipole moments that compare well for all three presented double dot models, so that laser intensities and durations are all in the same range. π-pulse durations, intensities, and the IR pulse delay time have been parametrically re-optimized as described in the previous section to obtain a maximal population transfer at each excitation step. Here again, for the initial UV pulse excitations of the top cluster, the transition dipole moments from the single nanocrystals are used to estimate the π-pulse conditions, see Eq. 13.

The right panel in Fig. 5 shows the exciton state population dynamics in the HAT-A DQD for the sequence: $|0\rangle \otimes |0\rangle \overset{UV}{\longrightarrow} |23\rangle \otimes |0\rangle \overset{transfer}{\longrightarrow} |0\rangle \otimes |23\rangle \overset{IR}{\longrightarrow} |0\rangle \otimes |7\rangle$. After UV excitation the ground state, $|0\rangle \otimes |0\rangle$ (purple), is virtually depopulated ($P_0 = 0.003$), while the intermediate excitonic state in the top cluster (dark blue) reaches a maximum population of $P(|23\rangle \otimes |0\rangle) = 0.931$ at $t = 0.374$ ps. The IR pulse sets in shortly before the exciton transfer to the bottom cluster is completed. There, the intermediate excitonic state in the bottom dot (light blue) shows a maximum population of $P(|0\rangle \otimes |23\rangle) = 0.890$ at around $t = 2$ ps. The intermediate states

involving predominantly the excitation $|23\rangle$ on either of the QDs are no pure states. In both cases, there is population in $|25\rangle \otimes |0\rangle$ and $|0\rangle \otimes |25\rangle$, however, only amounting to less than 0.05 each. This was already to be expected from the exciton state contributions to the eigenstates $|45\rangle$ and $|46\rangle$ listed in the middle of Fig. 5. Indeed, the dominant contributions in the intermediate states are more spread over multiple excitonic states than in the pyramidal Ge_7 core: $|23\rangle \otimes |0\rangle$ and $|0\rangle \otimes |23\rangle$ with only about $c = |0.69|$, $|25\rangle \otimes |0\rangle$ and $|0\rangle \otimes |25\rangle$ with $c = |0.15|$, compared to $c = |0.04|$ for $|21\rangle \otimes |0\rangle$ and $|0\rangle \otimes |21\rangle$ as the next dominant contribution. After IR pulse excitation the target state (red) is populated by $P(|0\rangle \times |7\rangle) = 0.918$, while its counterpart in the top QD $|7\rangle \times |0\rangle$ (orange) stays virtually unpopulated. The final target state itself is not strongly coupled to any other excitonic states, as can be seen from the coefficients of eigenstates $|15\rangle$ and $|16\rangle$ in the red-boxed table of Fig. 5. The target population is found to be smaller than in the pyramidal Ge_7 core, mostly due to non-linear effects during excitation, resulting in the population of a number of higher excited states (black).

A similar population evolution is obtained in the DQD from HAT-B Ge cores. The bottom panel of Fig.6 shows the population dynamics due to UV pump and time delayed IR dump pulse excitation, following the same strategy as above: $|0\rangle \otimes |0\rangle \overset{\mathrm{UV}}{\longrightarrow} |9\rangle \otimes |0\rangle \overset{transfer}{\longrightarrow} |0\rangle \otimes |9\rangle \overset{\mathrm{IR}}{\longrightarrow} |0\rangle \otimes |3\rangle$. Again, the UV π-pulse depopulates the ground state $|0\rangle \otimes |0\rangle$ (purple) (0.004), while an exciton on the top cluster is created $P(|9\rangle \otimes |0\rangle) = 0.964$ (dark blue) after $t = 0.31$ ps. Re-optimizing the pump-dump time delay, the IR π-pulse starts slightly before the coherent transfer is completed, such that after $t = 2.5$ ps an excitonic population in the bottom cluster of $P(|0\rangle \otimes |9\rangle) = 0.95$ (light blue) is observed. These intermediate states are as well mixed excitonic states, therefore, also populations in $|10\rangle \otimes |0\rangle$ and $|0\rangle \otimes |10\rangle$ are obtained. The IR pulse then de-excites the bottom cluster such that in the target state of the bottom QD (red) a population of $P(|0\rangle \times |3\rangle) = 0.922$ is achieved. The reduced efficiency for the target state population is here again mostly due to some excitation to higher excited states (black). However, the state $|3\rangle \times |0\rangle$ on the top QD is not at all populated, as desired.

These population dynamics in both HAT-A and HAT-B compare well with the pump-dump

simulations in DQDs based on the pyramidal Ge_7 structure. Such similarities have their origin in the types of excitations addressed by the lasers. As a quantitative measure of the similarities, the NTO densities for the intermediate and final excitons are computed and presented in the left panels of Figs. 5, 6, and 4 for the three cases studied. For all selected excitonic states in the three model QDs, localized holes at the Ge cores are observed (grey isosurfaces). This confirms the hole-trapping character of the excitations. The IR dump pulse are also not found to cause significant delocalization of the hole. However, the NTO density for the electron (blue isosurfaces) shows larger differences between all considered clusters. The electron in the intermediate state used for HAT-A, as shown on the top left of Fig.5, is located in the first silicon shell below the Ge_{11} QD. This is similar to the electron distribution in the target state of the pyramidal Ge_7 case (c.f. Fig. 4). In the case of DQDs based on the HAT-B structure, the electron remains delocalized through both pump and dump steps. This is a strong indication that the permanent dipole moment is not alone responsible for the energetic splitting between pairs of excitonic states, which serves as a driving force for the transfer exchange dynamics that is observed. The more delocalized nature of the particle is possibly also the reason for the stronger mixing among excitonic states for the intermediate state in both Ge_{11}-based DQDs, see central panels of Figs.5 and 6. Stronger mixing of the exciton character originates from the larger density of states coupled by their transition dipole moments. As a consequence, this seems to indicate that the multi-excitonic character of the eigenstates is intimately related to their energy splitting, which directly relates to the transfer rates. This induces faster exchange between the intermediate states on faster timescales in the Ge_{11}-based DQD cases as compared to the Ge_7 cluster. Indeed, exciton transfer between the stacked DQDs based on Ge_{11} is about twice as fast for the pyramidal case, and maximum population in the target states is obtained in 2.7 ps and 3 ps for HAT-A and HAT-B, respectively.

Conclusions and outlook

We have simulated laser-controlled electron-hole localization in pairs of stacked, coupled germanium/silicon quantum dots with various sizes in a symmetric donor-acceptor configuration. A Frenkel exciton model is constructed and parametrized from first principles using time-dependent density functional theory calculations. The atomistic treatment shows that a reduced-size DQD does exhibit similar features of the hole-trapped excitonic states in larger self-assembled Ge/Si nanostructures described by others.[42–44] Laser-induced many-electron dynamics calculations in the donor-acceptor Frenkel exciton model were carried out by means of the explicitly time-dependent hybrid TDDFT/CI method. To achieve long-lived hole trapping in a given QD a UV/IR pump-dump pulse sequence was designed. First, a UV laser excitation is optimized to create an exciton localized on the topmost QD. After some time delay, a second pulse in the IR regime is used to dump and localize an exciton in the bottom QD.

Three selected symmetric DQDs systems were studied: a pyramidal Ge_7 cluster, and two Ge_{11}, each surrounded by two wetting silicon shells and saturated by hydrogen atoms. The smaller pyramidal DQD system showed the highest population transfer efficiency and hole trapping performance in the target of the bottom QD $|0\rangle \otimes |6\rangle = 0.954$. This efficiency was found to come at longer times, 6 ps, though, due to the relative long time required for the exciton exchange between the QDs after initial excitation by the UV pump pulse. This means that the pump-dump strategy could be hampered by dissipation in such small DQDs.[53] A slight increase in the size of the quantum dots seems to improve this situation, due to an increased density of excited states. Our atomistic investigations of the intermediate and target state characters reveal that the hole remains trapped at all times while the particles are delocalized. Further, it indicates that the multi-excitonic character is probably responsible for the faster exciton transfer in the larger DQDs. Therefore, the larger QDs would make better candidates when including electron-phonon effects, since the overall dynamics is then faster.

In the system based on the so-called HAT-A structure, the fastest exciton transfer of about 2 ps is observed, leading to relatively fast hole trapping in the target QD. In comparison, a

DQD system based on QD fragments of the same size but with different shapes, labelled HAT-B, showed a slightly increased transfer time of about 2.5 ps. However, high excited states are involved in the pump-dump dynamics for HAT-A than for HAT-B, where only low-lying excitations where involved in the population dynamics. It demonstrates that even marginal changes in the connectivity and in the atomic structure of QD fragments can have non-negligible effects on the laser-driven many-electron dynamics. In particular, higher excited states are typically shorter-lived and they are expected to be more strongly coupled with the silicon environment. This latter coupling could be included in the theoretical treatment as an ionization process, *i.e.*, the loss of an electron to the silicon bulk. The TDCI methodology used here is amenable to the inclusion of ionization, with the used complex absorbing potentials in energy space[75] and in real space.[76] Proper treatment of this electron-loss process would allow to treat subsequent reactions, such as inter-Coulombic decay.[38,39]

As a general conclusion, since the Ge/Si quantum dots are self-assembled, there is only a little degree of control over their sizes and shapes. This implies that an experimental realization of the pump-dump scenario described here would necessarily be non-optimal for a large number of DQDs, although optimal for a given member of this ensemble. However, the mechanistic findings discussed in the present work can be transferred to other types of double quantum dots systems, such as QDs in solution, where the pump-transfer-dump strategy could be used to trap long-lived particle or hole states.

Acknowledgement

Volkswagen Foundation – Freigeist Fellowship no 89525 for finacial support. J.C.T. and P.K. is grateful to Beate Paulus for continuous support. The compute cluster of the Helmholtz-Zentrum Berlin and the Scientific Computing Services Unit of the Zentraleinrichtung für Datenverarbeitung (ZEDAT) at Freie Universität Berlin for computational time. Dr. Gunter Hermann and Dr. Fabian Weber are acknowledged for technical support and fruitful scientific discussions.

References

(1) Ekimov, A. I.; Efros, A. L.; Onushchenko, A. A. Quantum size effect in semiconductor microcrystals. *Solid State Commun.* **1985**, *56*, 921.

(2) Reed, M. A. Quantum Dots. *Sci. Am.* **1993**, *268*, 118.

(3) Rossetti, R.; Ellison, J. L.; Gibson, J. M.; Brus, L. E. Size effects in the excited electronic states of small colloidal CdS crystallites. *J. Chem. Phys.* **1984**, *80*, 4464.

(4) Alivisatos, A. P. Semiconductor Clusters, Nanocrystals, and Quantum Dots. *Science* **1996**, *271*, 933.

(5) Bimberg, D. *Semiconductor Nanostructures*; Springer, 2008.

(6) van der Wiel, W. G.; De Franceschi, S.; Elzerman, J. M.; Fujisawa, T.; Tarucha, S.; Kouwenhoven, L. P. Electron Transport through double quantum dots. *Rev. Mod. Phys.* **2002**, *75*, 1.

(7) Salfi, J.; Roddaro, S.; Ercolani, D.; Sorba, L.; Savelyev, I.; Blumin, M.; Ruda, H. E.; Beltram, F. Electronic properties of quantum dot systems realized in semiconductor nanowires. *Semicond. Sci. Technol.* **2010**, *25*, 024007.

(8) Mochalin, V. N.; Shenderova, O.; Ho, D.; Gogotsi, Y. The properties and applications of nanodiamonds. *Nat. Nanotechnol.* **2012**, *7*, 11–23.

(9) Alivisatos, P. Colloidal quantum dots. From scaling laws to biological applications. *Pure Appl. Chem.* **2000**, *72*, 3.

(10) Roddaro, S.; Pescaglini, A.; Ercolani, D.; Sorba, L.; Beltram, F. Manipulation of electron orbitals in hard-wall InAs/InP nanowire quantum dots. *Nano Lett.* **2011**, *11*, 1695.

(11) Eberl, K.; Lipinski, M.; Manz, Y.; Winter, W.; Jin-Phillipp, N.; Schmidt, O. Selfassembling quantum dots for optoelectronic devices on Si and GaAs. *Physica E* **2001**, *9*, 164 – 174.

(12) Kodera, T.; van der Wiel, W.; Ono, K.; Sasaki, S.; Fujisawa, T.; Tarucha, S. High-frequency manipulation of few-electron double quantum dots - toward spin qubits. *Phys. E* **2004**, *22*, 518.

(13) Zallo, E.; Atkinson, P.; Wang, L.; Rastelli, A.; Schmidt, O. G. Epitaxial growth of lateral quantum dot molecules. *Phys. Stat. Sol. B* **2012**, *249*, 702.

(14) Yakimov, A. I.; Kirienko, V. V.; Armbrister, V. A.; Bloshkin, A. A.; Dvurechenskii, A. V. Electronic States in Vertically Ordered Ge/Si Quantum Dots Detected by Photocurrent Spectroscopy. *Phys. Rev. B* **2014**, *90*, 035430.

(15) Maimon, S.; Finkman, E.; Bahir, G.; Schacham, S. E.; Garcia, J. M.; Petroff, P. M. Intersublevel transition in InAs/GaAs quantum dots infrared photodetectors. *Appl. Phys. Lett.* **1998**, *73*, 2003.

(16) Shen, J.; Zhu, Y.; Yang, X.; Li, C. Graphene quantum dots: emergent nanolights for bioimaging, sensors, catalysis and photovoltaic devices. *Chem. Commun.* **2012**, *48*, 3686.

(17) Vrijen, R.; Yablonovitch, E.; Wang, K.; Jiang, H. W.; Balandin, A.; Roychowdhury, V.; Mor, T.; DiVincenzo, D. Electron-spin-resonance transistors for quantum computing in silicon-germanium heterostructures. *Phys. Rev. A* **2000**, *62*, 012306.

(18) Ladd, T. D.; Jelezko, F.; Laflamme, R.; Nakamura, Y.; Monroe, C.; O'Brien, J. L. Quantum computers. *Nature* **2000**, *464*, 45.

(19) Wang, K.; Liu, J.; Jin, G. Self-Assembled Ge Quantum Dots on Si and their Applications. *J. Cryst. Growth* **2002**, *237-239*, 1892–1897.

(20) Stoffel, M.; Denker, U.; Schmidt, O. G. Electroluminescence of Self-Assembled Ge Hut Clusters. *Appl. Phys. Lett.* **2003**, *82*, 3236 – 3238.

(21) Caruge, J. M.; Halpert, J. E.; Wood, V.; Bulović, V.; Bawendi, M. G. Colloidal quantum-dot light-emitting diodes with metal-oxide charge transport layers. *Nat. Photonics* **2008**, *2*, 247.

(22) Bitnar, B. Silicon, Germanium and Silicon/Germanium Photocells for Thermophotovoltaics Applications. *Semicond. Sci. Technol.* **2003**, *18*, S221–S227.

(23) Kurzmann, A., A. Ludwig; Wieck, A. D.; Lorke, A.; Geller, M. Auger Recombination in Self-Assembled Quantum Dots: Quenching and Broadening of the Charged Exciton Transition. *Nano Lett.* **2016**, *16*, 3367.

(24) Larsson, K.; Tian, Y. Effect of surface termination on the reactivity of nano-sized diamond particle surfaces for bio applications. *Carbon* **2018**, *134*, 244.

(25) Yakimov, A. I.; Dvurechenskii, A. V.; Nikiforov, A. I.; Bloshkin, A. A.; Nenashev, A. V.; Volodin, V. A. Electronic states in Ge/Si quantum dots with type-II band alignment initiated by space-charge spectroscopy. *Phys. Rev. B* **2006**, *73*, 115333.

(26) Reiss, P.; Protiere, M.; Li, L. Core/shell semiconductor nanocrystals. *small* **2009**, *5*, 154 – 168.

(27) Weissker, H.-C.; Ning, N.; Bechstedt, F.; Vach, H. Luminescence and Absorption in Germanium and Silicon Nanocrystals: The Influence of Compression, Surface Reconstruction, Optical Excitation, and Spin-Orbit Splitting. *Phys. Rev. B* **2011**, *83*, 125413.

(28) Yakimov, A. I.; Dvurechenskii, A. V.; Volodin, V. A.; Efremov, M. D.; Nikiforov, A. I.; Mikhalyov, G. Y.; Gatskevich, E. I.; Ivlev, G. D. Effect of Pulsed Laser Action on Hole-Energy Spectrum of Ge/Si Self-Assembled Quantum Dots. *Phys. Rev. B* **2005**, *72*, 115318.

(29) Hermann, G.; Tremblay, J. C. Laser-Driven Hole Trapping in a Ge/Si Core-Shell Nanocrystal: An Atomistic Configuration Interaction Perspective. *J. Phys. Chem. C* **2015**, *119*, 25606–25614.

(30) Chen, W.-Y.; Chang, W.-H.; Chou, A.-T.; Hsu, T.-M.; Chen, P.-S.; Pei, Z.; Lai, L.-S. Optical Properties of Stacked Ge/Si Quantum Dots with Different Spacer Thickness Grown by Chemical Vapor Deposition. *Appl. Surf. Sci.* **2004**, *224*, 148 – 151.

(31) Gawarecki, K.; Machnikowski, P.; Kuhn, T. Electron states in a double quantum dot with broken axial symmetry. *Phys. Rev. B* **2014**, *90*, 085437.

(32) Müller, K.; Bechtold, A.; Ruppert, C.; Zecherle, M.; Reithmaier, G.; Bichler, M.; Krenner, H. J.; Abstreiter, G.; Holleitner, A. W.; Villas-Boas, J. M. et al. Electrical Control of Interdot Electron Tunneling in a Double InGaAs Quantum-Dot Nanostructure. *Phys. Rev. Lett.* **2012**, *108*, 197402.

(33) Ardelt, P.-L.; G recki, K.; Müller, K.; Waeber, A. M.; Bechtold, A.; Oberhofer, K.; Daniels, J. M.; Klotz, F.; Bichler, M.; Kuhn, T. et al. *Phys. Rev. Lett.* **2015**, *116*, 077401.

(34) Chenu, A.; Scholes, G. D. Coherence in Energy Transfer and Photosynthesis. *Annual Review of Physical Chemistry* **2015**, *66*, 69–96, PMID: 25493715.

(35) Radler, J. J.; Lingerfelt, D. B.; Castellano, F. N.; Chen, L. X.; Li, X. Role of Vibrational Dynamics on Excited-State Electronic Coherence in a Binuclear Platinum Complex. *J. Phys. Chem. A* **2018**, *122*, 5071–5077, PMID: 29652504.

(36) Bockelmann, U.; Egeler, T. Exciton relaxation and radiative recombination in semiconductor quantum dots. *Phys. Rev. B* **1993**, *48*, 17637.

(37) Ferreira, R.; Bastard, G. Evaluation of some scattering times for electrons in unbiased and biased single- and multiple-quantum-well structures. *Phys. Rev. B* **1989**, *40*, 1074.

(38) Bande, A. Acoustic Phonon Impact on the Inter-Coulombic Decay Process in Charged Quantum Dot Pairs. *Mol. Phys.* **2019**, *117*, 2014.

(39) Bande, A.; Gokhberg, K.; Cederbaum, L. S. Dynamics of Interatomic Coulombic Decay in Quantum Dots. *J. Chem. Phys.* **2011**, *135*, 144112.

(40) Reimann, S. M.; Manninen, M. Electronic structure of quantum dots. *Rev. Mod. Phys.* **2002**, *74*, 1283.

(41) Keren, K.; Stern, A.; Sivan, U. The different effect of electron-electron interaction on the spectrum of atoms and quantum dots. *Eur. Phys. J. B* **2000**, *18*, 311.

(42) Yakimov, A. I.; Stepina, N. P.; Dvurechenskii, A. V.; Nikiforov, A. I.; Nenashev, A. V. Excitons in charged Ge/Si type-II quantum dots. *Semicond. Sci. Technol.* **2000**, *15*, 1125.

(43) Yakimov, A. I.; Nikiforov, A. I.; Dvurechenskii, A. V. Localization of electrons in multiple layers of self-assembled GeSi/Si islands. *Appl. Phys. Lett.* **2006**, *89*, 163126.

(44) Yakimov, A. I.; Mikhalyov, G. Y.; Dvurechenskii, A. V.; Nikiforov, A. I. Hole states in Ge/Si quantum-dot molecules produced by strain-driven self-assembly. *J. Appl. Phys.* **2007**, *102*, 093714.

(45) de Oliveira, E. L.; Albuquerque, E. L.; de Sousa, J. S.; Farias, G. A.; Peeters, F. M. Configuration-Interaction Excitonic Absorption in Small Si/Ge and Ge/Si Core/Shell Nanocrystals. *J. Phys. Chem. C* **2012**, *116*, 4399–4407.

(46) Krause, P.; Klamroth, T.; Saalfrank, P. Molecular response properties from explicitly time-dependent configuration interaction methods. *J. Chem. Phys.* **2007**, *127*, 034107.

(47) Krause, P.; Klamroth, T. Dipole switching in large molecules described by explicitly time-dependent configuration interaction. *J. Chem. Phys.* **2008**, *128*, 234307.

(48) Sonk, J. A.; Schlegel, H. B. TD-CI Simulation of the Electronic Optical Response of Molecules in Intense Fields: Comparison of DFT Functionals and EOM-CCSD. *J. Phys. Chem. A* **2011**, *115*, 11832–11840.

(49) White, A. F.; Heide, C. J.; Saalfrank, P.; Head-Gordon, M.; Luppi, E. Computation of high-harmonic generation spectra of the hydrogen molecule using time-dependent configuration-interaction. *Molecular Physics* **2016**, *114*, 947–956.

(50) Ulusoy, I. S.; Stewart, Z.; Wilson, A. K. The role of the CI expansion length in time-dependent studies. *J. Chem. Phys.* **2018**, *148*, 014107.

(51) Lestrange, P. J.; Hoffmann, M. R.; Li, X. In *Novel Electronic Structure Theory: General Innovations and Strongly Correlated Systems*; Hoggan, P. E., Ed.; Advances in Quantum Chemistry; Academic Press, 2018; Vol. 76; pp 295–313.

(52) Li, X.; Govind, N.; Isborn, C.; DePrince, A. E.; Lopata, K. Real-Time Time-Dependent Electronic Structure Theory. *Chemical Reviews* **2020**, *120*, 9951–9993, PMID: 32813506.

(53) Klinkusch, S.; Tremblay, J. C. Resolution-of-identity stochastic time-dependent configuration interaction for dissipative electron dynamics in strong fields. *J. Chem. Phys.* **2016**, *144*, 184108.

(54) Hermann, G.; Pohl, V.; Tremblay, J. C. An open-source framework for analyzing N-electron dynamics. II. Hybrid density functional theory/configuration interaction methodology. *J. Comput. Chem.* **2017**,

(55) Hoerner, P.; Lee, M. K.; Schlegel, H. B. Angular dependence of strong field ionization of N2 by time-dependent configuration interaction using density functional theory and the Tamm-Dancoff approximation. *J. Chem. Phys.* **2019**, *151*, 054102.

(56) Tremblay, J. C.; Klamroth, T.; Saalfrank, P. Time-dependent configuration interaction calculations of laser-driven dynamics in presence of dissipation. *J. Chem. Phys.* **2008**, *129*, 084302.

(57) Tremblay, J. C.; Klinkusch, S.; Klamroth, T.; Saalfrank, P. Dissipative many-electron dynamics of ionizing systems. *J. Chem. Phys.* **134**, *2011*, 044331.

(58) Sonk, J. A.; Schlegel, H. B. TD-CI Simulation of the Strong-Field Ionization of Polyenes. *J. Phys. Chem. A* **2012**, *116*, 7161–7168.

(59) Klinkusch, S.; Tremblay, J. C. Resolution-of-identity stochastic time-dependent configuration interaction for dissipative electron dynamics in strong fields. *J. Chem. Phys.* **2016**, *144*, 184108.

(60) Martin, R. L. Natural transition orbitals. *J. Chem. Phys.* **2003**, *118*, 4775–4777.

(61) Tremblay, J. C.; Klinkusch, S.; Klamroth, T.; Saalfrank, P. Dissipative many-electron dynamics of ionizing systems. *J. Chem. Phys.* **2011**, *134*, 044311.

(62) Kühn, O. In *Handbook of Organic Materials for Electronic and Photonic Devices, Second Edition*; Ostroverkhova, O., Ed.; Woodhead Publishing Limited: Cambridge, 2019; p 259.

(63) Binder, R.; Römer, S.; Wahl, J.; Burghardt, I. An analytic mapping of oligomer potential energy surfaces to an effective Frenkel model. *J. Chem. Phys.* **2014**, *141*, 014101.

(64) Binder, R.; Burghardt, I. First-principles description of intra-chain exciton migration in an oligo(para-phenylene vinylene) chain. II. ML-MCTDH simulations of exciton dynamics at a torsional defect. *J. Chem. Phys.* **2020**, *152*, 204120.

(65) Förster, T. Zwischenmolekulare Energiewanderung und Fluoreszenz. *Annalen der Physik* **1948**, *437*, 55–75.

(66) Green, M. A.; Keevers, M. J. Optical properties of intrinsic silicon at 300 K. *Progress in Photovoltaics: Research and Applications* **1995**, *3*, 189–192.

(67) Green, M. A. Self-consistent optical parameters of intrinsic silicon at 300K including temperature coefficients. *Solar Energy Materials and Solar Cells* **2008**, *92*, 1305–1310.

(68) Schäfer, A.; Horn, H.; Ahlrichs, R. Fully optimized contracted Gaussian basis sets for atoms Li to Kr. *J. Chem. Phys.* **1992**, *97*, 2571–2577.

(69) Weigend, F.; Ahlrichs, R. Balanced basis sets of split valence, triple zeta valence and quadruple zeta valence quality for H to Rn: Design and assessment of accuracy. *Phys. Chem. Chem. Phys.* **2005**, *7*, 3297–3305.

(70) A Development of University of Karlsruhe and Forschungszentrum Karlsruhe GmbH, 1989-2007, TURBOMOLE GmbH. **since 2007**,

(71) Neese, F. The ORCA program system. *Comp. Mol. Sci.* **2012**, *2*, 73–78.

(72) Hermann, G.; Pohl, V.; Tremblay, J. C.; Paulus, B.; Hege, H.-C.; Schild, A. ORBKIT: A modular python toolbox for cross-platform postprocessing of quantum chemical wavefunction data. *J. Comput. Chem.* **2016**, *37*, 1511–1520.

(73) Pohl, V.; Hermann, G.; Tremblay, J. C. An open-source framework for analyzing N-electron dynamics. I. Multideterminantal wave functions. *J. Comput. Chem.* **2017**, *38*, 1515–1527.

(74) Tremblay, J. C.; Carrington, T. Using preconditioned adaptive step size Runge-Kutta methods for solving the time-dependent Schrödinger equation. *J. Chem. Phys.* **2004**, *121*, 11535–11541.

(75) Klinkusch, S.; Saalfrank, P.; Klamroth, T. A heuristic model within tdci theory. *J. Chem. Phys.* **2009**, *131*, 114304.

(76) Krause, P.; Sonk, J.; Schlegel, H. B. Strong field ionization rates simulated with time-dependent configuration interaction and an absorbing potential. *J. Chem. Phys.* **2014**, *140*, 174113.

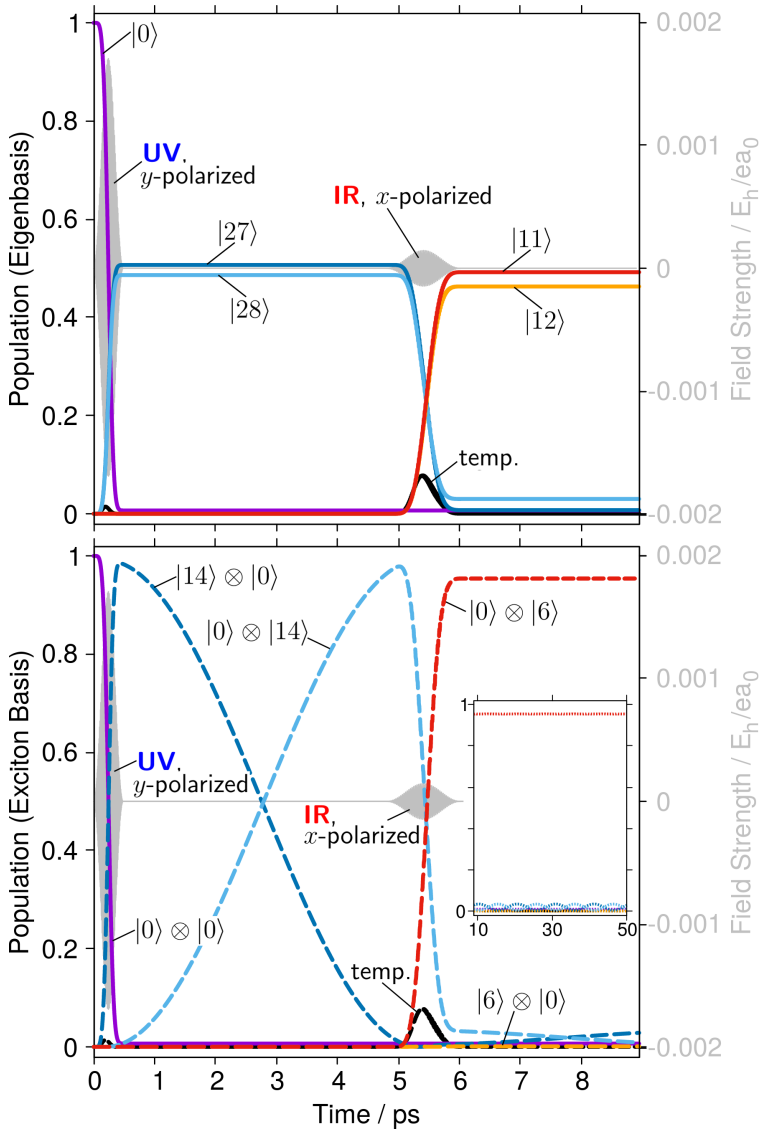

Figure 3: Exciton population dynamics in coupled Ge_7/Si double quantum dots due to excitation and de-excitation by a UV+IR pulse sequence for which the pulse is given as a gray-shaded area. Top: time-dependent eigenstates populations; Bottom: population evolution of corresponding exciton states, the inset shows these populations for times up to 50 ps. The dominant states are indicated by their kets, during the IR pulse a black lines shows temporarily occupied other states (temp.). Laser parameters: UV: y-polarized cos-squared pulse $f_{0,y} = 0.0017$ E_h/ea_0, $\hbar\omega_{0,1} = 0.1473$ E_h (4.0071 eV), $2\sigma_1 = 483.8$ fs centered at $t_{p,1} = 241.9$ fs; IR: x-polarized cos-squared $f_{0,x} == 0.000145$ E_h/ea_0 $\hbar\omega_{0,2} = 0.0057$ E_h (0.154 eV), $2\sigma_2 = 1209.44$ fs centered at $t_{p,2} = 5442.48$ fs.

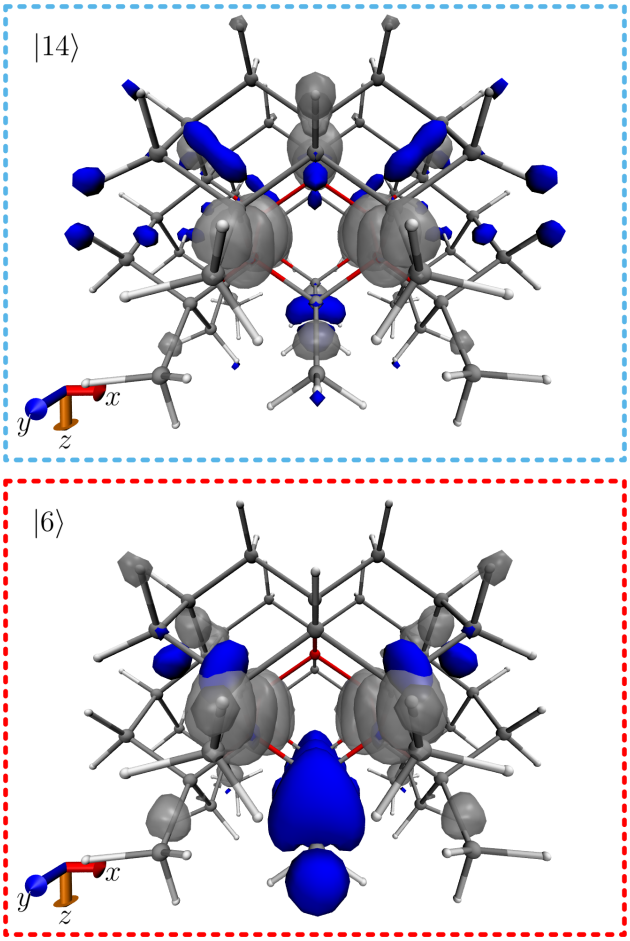

Figure 4: Natural transition orbital densities for a single pyramidal Ge/Si core/shell nanocrystal (red/silver spheres) elaborating the hole-trapped state involved after UV excitation (top) and the electron-hole localization after IR excitation (bottom). Blue isosurfaces represent the electron densities and the transparent grey isosurfaces the densities of the hole (the isosurface value was set to 0.0007 a_0^{-3}).

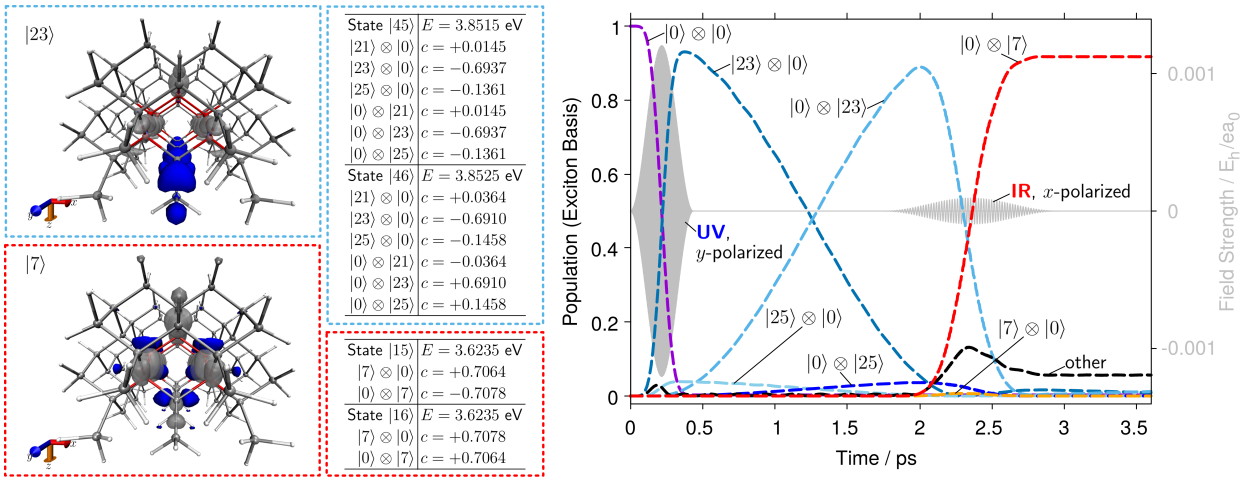

Figure 5: Summary of the exciton characterization and population dynamics in a DQD of two HAT-A Ge/Si core/shell nanocrystals. On the left, the NTO densities are displayed for a single nanocrystal (blue/silver isosurfaces represent the electron/hole NTO densities at isosurface value 0.0007 a_0^{-3}). The NTO densities in the blue boxes corresponds to the intermediate UV-excited state, for which the composition is given in the center of the figure. The NTO densities in the red boxes corresponds to the target state after IR dumping. Dynamics subsequent due to excitation with two cos-squared π-pulses is shown on the right-hand-side of the figure in exciton basis representation. Parameters for the cos-squared π-pulses: UV: y-polarized, $I_{\max} = 50.536$ GW/cm^2, $\hbar\omega_{0,1} = 3.852$ eV, $2\sigma_1 = 435.4$ fs centered at $t_{p,1} = 217.7$ fs; IR: x-polarized $I_{\max} = 0.317$ GW/cm^2, $\hbar\omega_{0,2} = 0.228$ eV, and $2\sigma_2 = 1.209$ ps centered at $t_{p,2} = 2.35$ ps.

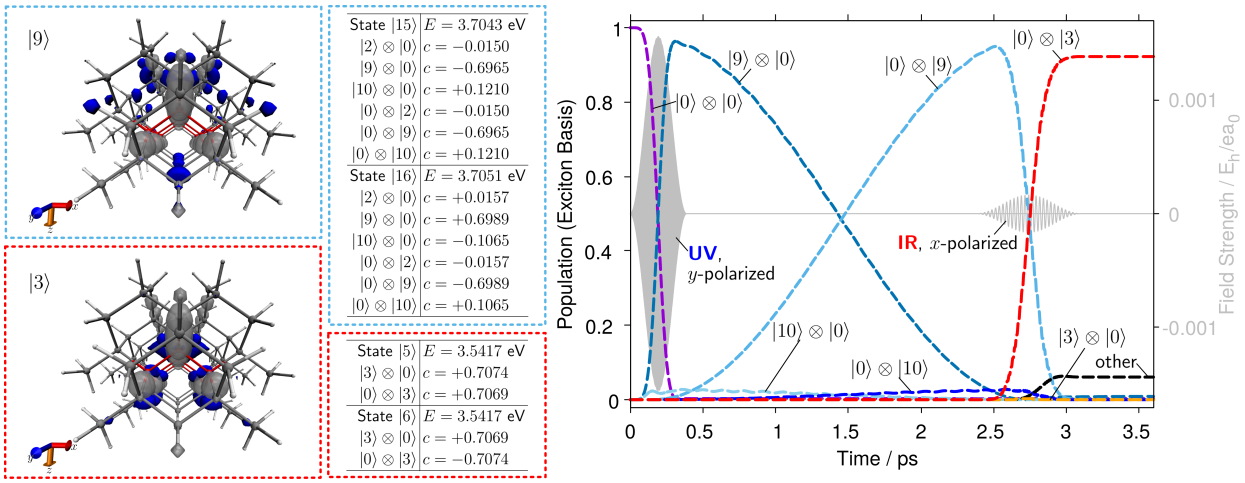

Figure 6: Same as in Fig. 5 for a DQD composed of two HAT-B Ge/Si core/shell nanocrystals. Parameters for the cos-squared π-pulses: UV: y-polarized, $I_{\max} = 85.014$ GW/cm^2, $\hbar\omega_{0,1} = 3.705$ eV, $2\sigma_1 = 387.0$ fs centered at $t_{p,1} = 193.5$ fs; IR: x-polarized with $I_{\max} = 0.948$ GW/cm^2, $\hbar\omega_{0,2} = 0.163$ eV, and $2\sigma_2 = 725.7$ fs centered at $t_{p,2} = 2741.4$ fs.

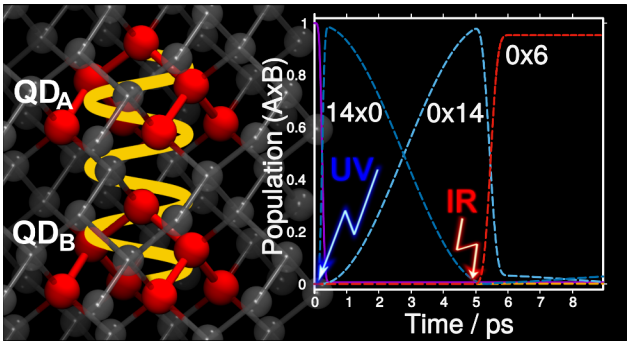

Figure 7: TOC graphic